

Addressing Known Challenges in Solar Flare Forecasting I: Limb-Flare Prediction with a 4π Full-Heliosphere Framework

K. D. Leka¹, Eric L. Wagner¹, Lisa Upton², Bibhuti Kumar Jha², Kiran Jain³,
Sara Petty¹

¹NorthWest Research Associates, Boulder, Colorado, USA.

²Southwest Research Institute, Boulder, Colorado, USA.

³National Solar Observatory, Boulder, Colorado, USA.

arXiv:2601.05209v1 [astro-ph.SR] 8 Jan 2026

Key Points:

- Solar flare forecasting generally fails to forecast flares near or just-beyond the solar limb.
- We present a new full-heliosphere forecasting method that combines a surface flux-transport model and far-side helioseismology.
- Within this proof of concept framework, geo-effective limb flares were forecast with demonstrably improved performance.

Corresponding author: K. D. Leka, leka@nwra.com

Abstract

A demonstrated failure mode for operational solar flare forecasting is the inability to forecast flares that occur near, or just beyond, the solar limb. To address this shortcoming, we develop a “ 4π ” full-heliosphere event forecasting framework and evaluate its statistical classification ability against this specific challenge. A magnetic surface flux transport model is used to generate full-sun maps of the photospheric radial magnetic field from which active regions (ARs) are identified and tracked using a new labeling scheme that is observer-location agnostic and allows for post-facto modifications. Flare-relevant magnetic parameters couple to a “visibility” index that specifies AR location relative to the visible solar limb and expected flare detection. Flare labels are assigned according to peak Soft X-ray flux, and a statistical classification is performed using nonparametric discriminant analysis. A version where new or emerging ARs on the far (“invisible”) side of the Sun are incorporated into the model by way of far-side helioseismology, is also tested. We evaluate the new framework by its performance specifically on the limb areas using Brier Skill Score and ROC Skill Score, finding improvement at the 2σ level or less. However, we do find that the number of False Negatives, or “missed” forecasts decreases, and find strong evidence that the additional information provided by the far-side helioseismology can help predict near- and just-beyond-limb flares, particularly for East-limb events. While individual components of this framework could be improved, we demonstrate that a known failure mode for solar flare forecasting can be mitigated with available resources.

Plain Language Summary

Solar flares can occur anywhere there are concentrated magnetic fields on the Sun (active regions or sunspot groups). Predicting solar flares often uses the character of those magnetic fields to estimate the likelihood of a flare occurring. However, a significant fraction of solar flares that are visible from the Earth (thus potentially hazardous to our technological systems, especially communications) occur in regions where the magnetic field data becomes increasingly noisy and unreliable, or just beyond the edge of the Sun where we cannot see the magnetic fields at all. Forecasting for these particular flares is generally unsuccessful, thus identified as the “Limb-Flare Challenge”. We have developed a framework that uses physics-based modeling to create a map of the “ 4π ” or “full-Sun” (including the far-side, or unobserved part of the Sun), and test this new ability to address this specific forecasting challenge. Additionally, we quantify the improvements made when additional information is included from far-side helioseismology, a technique using Earth-visible data to detect strong magnetic fields on the far side of the Sun. We show that with this new “ 4π ” forecasting framework, and with the additional information about the far-side magnetic field, the number of limb-flares “missed” by forecasts can successfully decrease.

1 Introduction

The challenges of forecasting solar flares are well documented and discussed (e.g. Leka & Barnes, 2017; Leka et al., 2019a; Georgoulis et al., 2021). Recently, it was demonstrated that operational forecasting facilities can indeed provide positive skill against random- or climatology-based forecasts, as measured with multiple evaluation metrics (Leka et al., 2019a). On the research side, there has been a plethora of recent efforts to improve flare forecasts, the vast majority involve exploring machine-learning (ML) methods (34 refereed publications with titles that include “Solar Flare Forecasting” in just 2024 and 2025 thus far), though some investigate new data sources as well (Leka et al., 2023; Sun et al., 2023; Zbinden et al., 2024). Central to this activity is the increasing sample size of data, in large part from the Solar Dynamics Observatory facility (SDO; Pesnell et al., 2012) that has observed the visible solar disk almost continuously for over 15 years at

the time of this writing. Of the SDO instruments, the magnetic field data provided by the Helioseismic and Magnetic Imager (HMI; Scherrer et al., 2012; Couvidat et al., 2012; Schou et al., 2012; Centeno et al., 2014; Hoeksema et al., 2014) has been central to flare-forecasting research – in part due to the “Space Weather Active Region Patch Parameters” data product that is provided. This data product includes a small number of pre-computed parameters describing photospheric magnetic concentrations or HMI Active Region Patches (“HARPs”; Bobra et al., 2014) that are readily available as meta-data (Bobra et al., 2014). Interest in ML-based forecasting methods has become widespread, with many efforts exploring the efficacy of combining the SHARP parameters with different flavors of ML tools; improvement in forecasting capability have been reported, although cross-publication comparison of any particular metric must be done with care (see discussions in Barnes et al., 2016; Kubo, 2019; Leka et al., 2019a).

One specific performance gap was recently identified as being particularly difficult for present approaches to address: forecasting limb flares (Park et al., 2020). Due to the lack of photospheric magnetic field data or even white-light imaging towards the edge of, or beyond, the visible solar disk, algorithms generally cannot provide forecasts for active regions (ARs) located (or even suspected to be located) in these areas. Some facilities do produce extended validity-period forecasts, which could provide forecasts for an AR – but generally for no more than a day past the western limb-transit (*e.g.*, the 2- or 3-day forecasts available from NOAA/SWPC, DAFFS, and others; see Leka et al., 2019a, for descriptions). However, this option only addresses West-limb events. Solar flares that occur at, or just beyond, the visible East limb can also impact the Earth’s ionosphere, for example, if the Soft X-Rays (SXR) and [Extreme] Ultraviolet (E/UV) radiation from event-associated coronal loops are visible above the limb (see, *e.g.*, NOAA/Space Weather Prediction Center, 2024a).

A recent effort has attempted to address this challenge with a forecasting system based solely on images of E/UV emission, which can capture coronal loops that appear above the limb (Lee et al., 2024). However, this approach still relies on Sun-Earth-line data, and requires active-region-related emission to be present (meaning: an AR must be large enough, active enough, and close enough to the limb that the associated coronal loops are available for analysis).

Here we present a different approach: “ 4π ” event forecasting. The basic technique is to invoke a “full-Sun”, meaning both Earth-facing “visible” and far-side “not visible” or a 4π representation of the solar photospheric magnetic field. We parameterize identified ARs to quantitatively characterize their magnetic field distributions (as is common for forecasting methods), and evaluate a sample of labeled event-producing and event-quiet ARs using a statistical classifier such that future regions and their parameters can be labeled predictively. In this new framework of 4π full-Sun forecasting, we additionally (1) include information about far-side (invisible from the Earth) ARs identified with far-side helioseismology, and (2) provide forecasts for both “occulted” and near-limb regions as well as Earth-facing regions for which forecasts would otherwise be unavailable.

We describe the full methodology in Section 2, including the framework and input (both observational and modeling, near-side and far-side) to generate the 4π -Sun in Section 2.1, and describe a new AR referencing scheme for 4π analysis in Section 2.2. We describe the parameterizations in Section 2.3, the statistical approach and specific tests designed and carried out in Section 2.4, the results in Section 3 and finish with a discussion in Section 4.

2 Methodology

The 4π forecasting framework consists of essentially three parts: generating the full 4π solar surface magnetic field, identifying the ARs and parametrizing their magnetic

field distribution, and a statistical analysis of those parametrizations in the context of flare activity.

2.1 Generating the 4π Sun

The photospheric magnetic field on the full Sun (*vs.* the visible disk) is required input for numerous heliospheric models, including solar wind and heliospheric event propagation (*e.g.*, the Wang-Sheeley-Arge-ENLIL solar wind and CME propagation model; Arge et al., 2004; Odstrcil et al., 2004). This boundary input can be “built up” by way of creating synoptic or synodic input over the course of the ≈ 1 mo rotation period, but the information on the far side of the Sun is then necessarily very outdated. For a synchronic 4π map that represents the Sun at a given moment, surface flux transport models have been developed to assimilate Earth-facing photospheric magnetic field information, and then evolve the field according to modeled physics.

2.1.1 The Advection Flux Transport Model

Here we use the Advection Flux Transport model (AFT; Upton & Hathaway, 2014a, 2014b) to construct synchronic estimates of the solar photospheric magnetic flux over the entire Sun. In brief, data from Earth-facing sources are assimilated; in the present version HMI line-of-sight magnetic maps from the `hmi.M_720s` data series are used to estimate the radial component B_r using a “ μ -correction” (Svalgaard et al., 1978; Wang & Sheeley, 1992); (see also Leka et al., 2017, for discussion). The assimilation window is a weighted function that falls off radially from the center of the disk. This has the effect of de-emphasizing data near any visible solar limb, where magnetic field measurements are known to be problematic.

AFT then solves the radial component of the induction equation:

$$\frac{\partial B_r}{\partial t} + \nabla \cdot (\vec{u} B_r) = S(\theta, \phi, t) + \eta \nabla^2 B_r \quad (1)$$

where B_r is the radial magnetic field, \vec{u} denotes horizontal flows including convective and axisymmetric flows (differential rotation and meridional circulation), S is a magnetic source term (representing new flux added to the model), and η is a numerical diffusivity term. In our case, the induction equation is solved in 15 min time steps with HMI data assimilated hourly. The convective velocities are implemented using a spherical harmonic code that simulates cellular convective structures (of supergranular spatial scales and larger) that evolve in time. These convective cells have lifetimes that are inversely proportional to their sizes and they are advected with observed axisymmetric flows (Upton & Hathaway, 2014a). This convective simulation is used to generate a series of latitudinal and longitudinal flow maps with a 15-minute cadence, coinciding with the model time step. AFT maps generated with this configuration are referred to as AFT “Baseline” maps.

The 4π AFT maps are sampled at 0.352° in both latitude and longitude (corresponding to a map size of 512×1024 pixels), which is finer than most surface flux transport models, especially when serving as the inner boundary-input to global models. Here, we are in fact interested in the small-scale behavior and characteristics of ARs, hence the higher AFT spatial sampling is key. The AFT magnetic field maps are field-filled (unity fill fraction), and the magnitude of the signal is referred to in units of Gauss-equivalent Mx cm^{-2} to reflect this characteristic (and to be consistent with HMI data. For this experiment, we use AFT-generated maps created at a cadence of three times each day (00:00, 08:00, and 16:00 UT).

2.1.2 AFT Active-Region Detection

Active regions are the dominant source of all flares, particularly for larger flares. As such, we apply the following algorithm to detect concentrations of magnetic field in

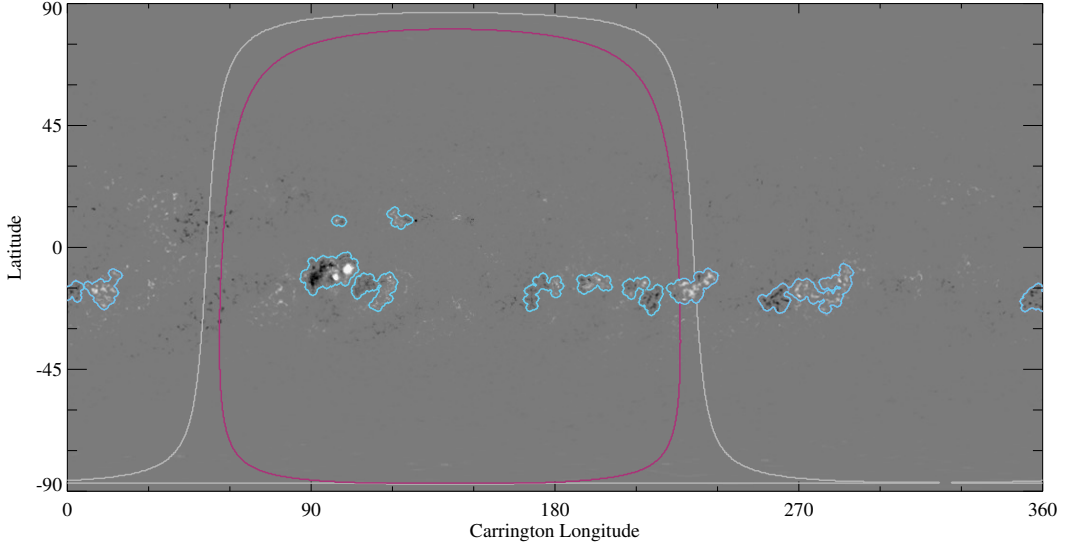


Figure 1. An example AFT full-Sun (or ‘4π’) magnetic field map on 2014.01.04 18:00 UT, scaled to $\pm 1,000 \text{ Mx cm}^{-2}$, with the solar limb (grey), the AFT assimilation window (magenta) and identified AFT active regions, or AFT-ARs (blue). Note that the b_0 -angle on this day is such that the south pole is slightly visible. In this example, the regions fully within the assimilation window would be assigned **Disk**, the two regions on the far-side (at $\text{CL}=[0^\circ, 280^\circ]$) would be assigned **Far**, and the region centered at $\text{CL} \approx 230^\circ$ that spans both the assimilation and limb terminators would be assigned **Occ**, or ‘‘occulted’’ (see Section 2.3.1 for details).

the AFT maps, which we denote as AFT active regions (AFT-ARs). This approach is an extension of the method proposed by Sreedevi et al. (2023).

First, an intensity threshold of 150 Mx cm^{-2} is applied to the image and pixels below this threshold are excluded. Second, a morphological closing operation, with a circular kernel of 4 pixels, is applied to fill the gaps between pixels separated by this threshold; this step also helps to join the positive and negative polarities of an AR bipole. Next, an area threshold of 20 pixels (roughly 4.5° 2 or approximately 6.6 Mm^2) is applied to exclude very small regions, based on the lower limits found using a frequency-distribution analysis of the regions detected to this point. Arguably this step may remove the very initial detection of growing regions, but the dominant effect is to remove small spurious detections. Finally, a moderate flux balance condition and flux threshold are applied primarily to eliminate plage regions and similar unipolar areas. Here, flux balance is defined as:

$$r = \frac{|\Phi^+ + \Phi^-|}{|\Phi^+ - \Phi^-|} \quad (2)$$

with Φ^+ , Φ^- being the total signed magnetic flux of positive and negative polarities, respectively. As such, a flux-balanced AR has $r = 0$ and fully unbalanced region (unipolar) produces $r = 1$. For the present rendition, we require an AR to have $r < 0.7$ (requiring no worse than $5 \times$ imbalance in flux between Φ^+ and Φ^-), and $\Phi > 5 \times 10^{19} \text{ Mx}$.

An example AFT map with identified regions is shown in Figure 1.

2.1.3 Far-Side Magnetograms from Far-Side Helioseismology

We have no direct and consistent observations of the Sun’s magnetic field beyond the limb of the Sun as seen from the ‘‘near-side’’, or the Sun-Earth line. However, the

Sun's magnetic field does evolve and new ARs continue to emerge on the “invisible” far-side of the Sun. Helioseismology can be used to infer activity that involves significant magnetic flux on the far side (Lindsey & Braun, 2000; Braun & Lindsey, 2001; González Hernández et al., 2007; González Hernández et al., 2010). For this experiment, we use helioseismic output (phase-shift maps) from the far-side processing pipeline of the Global Oscillation Network Group (GONG; Harvey et al., 1996; Jain et al., 2021). Each far-side phase-shift map is constructed by combining five successive phase-shift maps taken at 6 hr intervals over a 48 hr period. Twice-daily phase-shift maps at 00:00UT and 12:00UT are then converted to magnetic flux-density maps following González Hernández et al. (2007, 2014); MacDonald et al. (2015) on a grid of 180×360 pixels. The information on these maps are used to inform the AFT model of additional far-side magnetic flux emergence (as described below).

2.1.4 Far-Side Active Region Detection

To detect magnetic activity in far-side magnetic flux maps derived from GONG phase-shift data, we use a multi-step approach:

1. We first define a flux-density threshold for the selected GONG inferred flux-density maps using the relation $I_{\text{th}} = \bar{I} + 3\sigma(I)$, where \bar{I} and $\sigma(I)$ are calculated only over pixels where the inferred flux density is more than 0.1 Mx cm^{-2} (this is to avoid inversion-generated noise values). This is performed using the sigma clipping method *i.e.*, iteratively calculating the mean by removing the intensity values beyond 3σ (AstroPy Developers, 2025). Typical threshold values are of order 90 Mx cm^{-2} , with $\sigma(I) = 20$ after the sigma clipping. Any feature in the flux-density maps that exceeds this flux-density threshold is labeled as a candidate region.
2. We next ensure the persistence of a candidate region by examining the signal in the GONG magnetic flux map in either the previous observation or the next. To do this, candidate regions are first identified in these neighboring maps using a slightly relaxed threshold, *i.e.* $I_{\text{th}} = \bar{I} + 2\sigma(I)$. We then check for region overlap, and if the regions from either of the adjacent GONG flux-density maps overlap by more than 5 pixels, we confirm the persistence of the candidate region.
3. Once we identify a persistent candidate AR, we calculate its properties including latitude and Carrington longitude based on the flux-density- weighted spatial mean (a magnetic center-of-mass or MCOM approach), total magnetic flux, and maximum flux-density. We only accept candidate far-side ARs with a peak magnetic flux density of at least 250 Mx cm^{-2} , total magnetic flux greater than $5 \times 10^{20} \text{ Mx}$ and centroid latitude within the limits of the active zone defined as:

$$\ell = \ell_0 \exp\left(-\frac{T - T_0}{\tau}\right) \pm 20^\circ, \quad \ell_0 = \pm 28^\circ \text{ & } \tau = 90; \quad (3)$$

where ℓ_0 and thus ℓ is a signed latitude (that is, referring to both hemispheres), and $T - T_0$ is the number of months from the beginning of the solar cycle (Hathaway, 2011). The relevant parameters have been tuned to make the distribution of identified far-side ARs (in latitude and number) as consistent as possible to those observed on the near side of the Sun. The choice of 20° is based on the maximum width of the “butterfly wings” observed in near-side AR data over a complete solar cycle. To ensure robustness, a limit corresponding to 4 times the 1σ value in Hathaway (2011) Eqn. 9 was adopted.

Figure 2 (panels a, b, and c) provides a representative example of the process. The three panels show three consecutive far-side flux-density maps: Figure 2b represents the target map at the time of interest for identifying far-side ARs and Figures 2a, c are the far-side flux-density maps at $\pm 12\text{hr}$, used to verify the consistency of the ARs. Contours at all three times represent region candidates although candidates at the neighboring times

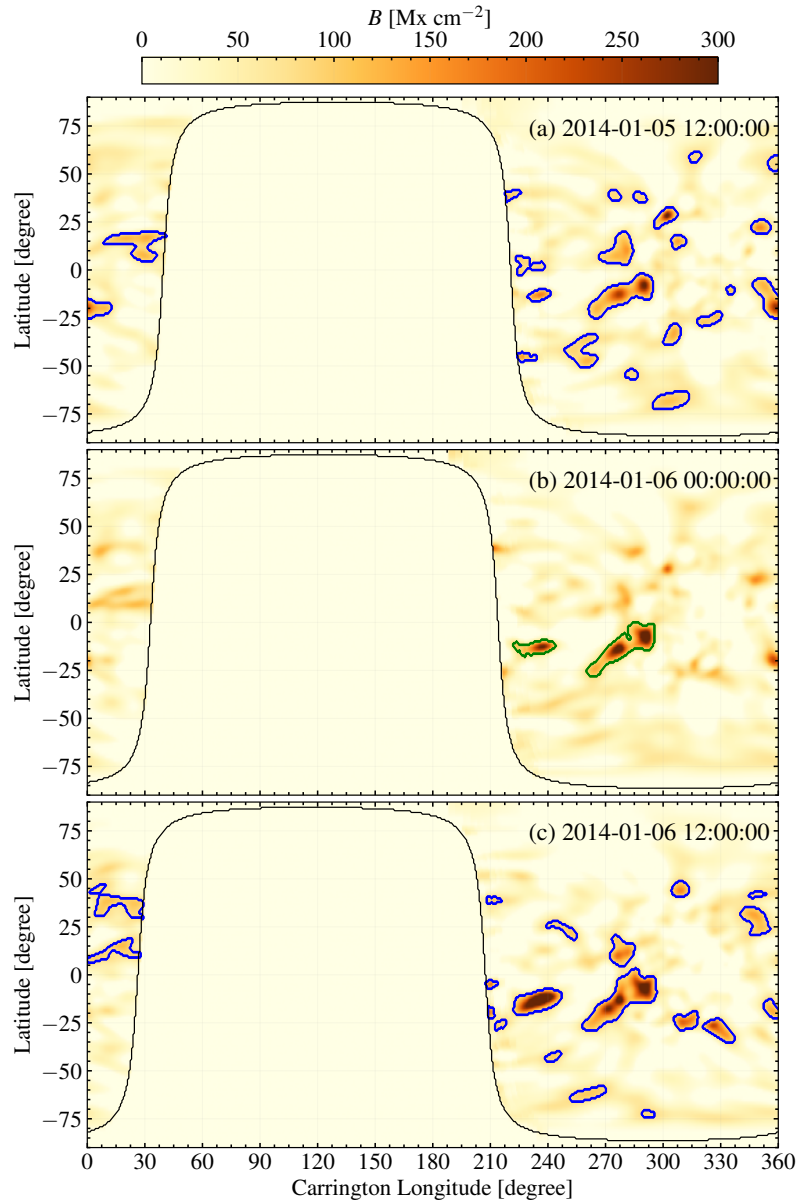


Figure 2. GONG flux-density maps for a target time (panel b, middle) and the prior map 12 hr prior (panel a, top) and the subsequent map 12hr later, scaled as shown. Blue contours (panel (a) at -12h and panel (c) at +12hr) identify the potential AR regions based on the relaxed threshold (see text for details); green contours in panel (b) identify the final set of far-side ARs that satisfy all the criteria for far-side ARs including the more stringent threshold applied for the target time to avoid noise.

($\pm 12\text{hr}$) are based on the relaxed threshold. The only AR candidates that satisfied all of the criteria are those with contours shown in Figure 2b, at the target time.

2.1.5 Far-Side Active Region Information Incorporation into AFT

Once the far-side ARs are identified on the GONG flux-density maps, the information needs to be incorporated in the AFT model. The steps for this are as follows:

1. A “region mask” is defined for each candidate AR by the contours described above. Because far-side AR candidates display considerable fluctuation in their location, we extend the mask by 10 pixels (10°) in longitude both East/West and 5 pixels (5°) in latitude both north/south. This mask is used to calculate the total flux in the same region using the already-modeled AFT map. If the total magnetic flux in the mask (for the far-side AR candidate) from the GONG flux-density map is greater than the total magnetic flux of the AFT map in same mask, we start the process of adding the far-side AR into AFT; otherwise it is excluded. This step is performed to ensure that we only add in new far-side ARs or flux from ARs with significant growth. Any subsequent AR decay is completely governed by the surface flux transport processes.
2. To add a candidate GONG-identified AR to AFT, we use the AR’s location and magnetic flux as derived from the GONG flux-density maps to construct an ideal bipolar region modeled as two 2-D Gaussian distributions of opposite-polarity magnetic flux, with standard deviation and amplitude tuned to match characteristics of HMI magnetograms. These simple dipoles are provided with the expected Joy’s law tilt according to latitude and Hale’s law for polarity orientation according to hemisphere (Hale et al., 1919). The flux *vs.* area relation (Sheeley, 1966; Mosher, 1977), and area *vs.* polarity separation distance relation (Hathaway & Upton, 2016), are used to determine the size and separation of the negative/positive polarity flux concentrations.
3. Tests indicated that simply using the estimated magnetic flux density from the GONG maps directly added too much flux to the AFT maps, as evidenced by the behavior of newly-inserted far-side ARs undergoing a sharp decrease in magnetic flux density once the AFT data-assimilation process corrected them with HMI data. As such, we calculate the fraction f of total magnetic flux from a GONG-identified AR that needs to be added into AFT with a new dipole, as

$$f = \frac{\alpha\Phi_{\text{Far}} - \Phi_{\text{AFT}}}{\alpha\Phi_{\text{Far}}}. \quad (4)$$

We have found upon initial analysis that the assimilation of newly inserted ARs was smoothest when $0.25 \leq \alpha \leq 0.35$, and thus assigned $\alpha = 0.3$. However, the present work is focused on shorter-term AR evolution and in fact α may be non-linear with magnetic flux density, AFT-based evolution prior to near-side assimilation, AR morphology, or even solar cycle phase. Further investigation is on-going but beyond the scope of this application.

The effect of adding far-side ARs, or adding magnetic flux to established ARs as they transit the far-side of the Sun, is to (unsurprisingly) increase the number of AFT-ARs above what is identified by AFT-Baseline, particularly on the Eastern limb.

2.2 Active-Region Tracking and Numbering

NOAA assigns sequential numbers to their identified ARs, as do the “HMI Active Region Patches” (HARPs Bobra et al., 2014), even though the two facilities have very different definitions of what constitutes an AR. Common to these two numbering schemes is that a region which disappears beyond the West limb as the Sun rotates and transits

the “far side” will be assigned a new number upon re-appearance on the East visible limb. This situation creates two sources of confusion: first, the same concentration of magnetic flux is assigned to multiple identities over its lifetime, and second, sequential numbering prohibits any incorporation of newly identified AR into the record, or even corrections made to the list *post facto*. As this project necessarily tracks ARs possibly over numerous solar rotations and includes ARs that may be first identified on the far side, a new region-labeling system is needed.

In this new “ 4π ” framework, once magnetic regions are identified by the methods described above (Sections 2.1.2, 2.1.4), they are assigned an identification and tracked using a modified AutoTAB (`autotabpy`) algorithm (Jha et al., 2021; Sreedevi et al., 2023; Jha, Sreedevi, et al., 2025). Newly identified ARs are labeled with a code (an “AFT-ID”) that specifies the date of first detection and the MCOM latitude and Carrington longitude. As an example, the AFT-AR with the ID “20121109TN11243” (or “AFT-ID”) first became an AFT-identified AR on 2012 November 09 at Latitude N11 Carrington Longitude 243. This identifier is an easily-parsable string and most importantly, unique; it does not need to change according to the relative location of the Earth. After running on more than 10 years of data, this system does not produce duplicates or conflicts and allows for modifications according to detection algorithm particulars, without jeopardizing the numbering scheme.

AFT-ARs are linked, then, to their corresponding NOAA AR numbers by way of the latter’s Latitude and Carrington Longitude, within a 10° window. As such, a single AFT-ID can have multiple NOAA ARs associated with it, not unlike the HARP-IDs. AFT-ARs that are in close proximity are combined, or absorbed, into the biggest and/or oldest match – again, within 10° . This process effectively treats multiple AFT-ARs (as initially identified) that would match to an identical NOAA AR number as a single AFT-AR. Additionally, since AFT-ARs may in fact disappear and re-appear with a new AFT-ID (due to varying noise levels and subtle challenges to temporal continuity), a single NOAA AR may in fact be associated with more than one AFT-ID over the course of their respective lifetimes (this is the case for NOAA-AR 12205, discussed in Section 3.1, below). It is not evident in the available NOAA documentation exactly when a numbered NOAA AR that transits the full far side is assigned a new number once it appears at the East solar limb, but by associating each unique AFT-AR with any and all NOAA AR numbers, limb- and beyond-limb events can be correctly labeled (see Section 2.4.2).

2.3 Parametrization

The magnetic field distributions of the AFT-ARs are parametrized with a focus on describing the character of the AR in the context of flare productivity. From experience developing DAFFS-G (Leka et al., 2018, 2019a, see www.nwra.com/DAFFS) where flare prediction is based on the line-of-sight magnetic field from GONG, the parameters used here include those that have shown efficacy in this context. It must be emphasized that we are *not* trying to achieve the “best” forecasts, but instead provide a “proof of concept” for 4π forecasts.

2.3.1 Identification, location, and visibility

The identification parameters include the AFT-AR ID (transformed into a 32-bit integer code for the Fortran code in the statistical analysis, see Section 2.4.1), and a code for whether the data were assimilated into AFT from the HMI input. The location parameters include not just the MCOM Latitude / Carrington Longitude of the AFT-AR, but the Stonyhurst Latitude / Longitude, extended to $\pm 180^\circ$ (0° being central meridian), and the cosine of the observing angle $\mu = \cos(\theta) = \cos(\text{Stonylat.}) \cos(\text{StonyLong.})$ such that $\mu < 0$ denotes beyond-visible MCOM AFT-AR locations.

Table 1. Visibility Labels

Moniker	Assignment	Description
“Disk”	On-disk	Fully visible from Earth, < 5% of area beyond AFT assimilation window
“Occ”	Occulted, Limb	> 5% area beyond AFT assimilation window, but still expected to be visible due to size and location (Eqn. 5)
“Far”	Far-side, Invisible	Not visible from Earth due to size and location

Related to the location of an AFT-AR is a “visibility” parameter assigned to the region (Figure 3, Table 1). On-disk (“Disk”) ARs are fully visible from Earth-side viewing and have more than 95% of the AFT-AR boundary falling within the AFT assimilation window that effectively cuts off at $\mu \approx 0.1$ ($\theta \approx 84^\circ$). Occulted or Limb ARs (“Occ”) will either (1) have more than 5% of its AFT-AR boundary beyond the AFT assimilation window or (2) be located fully beyond the visible limb but still at a location at which, given its size, the region’s associated coronal loops would be expected to be visible from the Earth during an energetic event (Figure 3). The first boundary thus assigns **Occ** to regions that may be visually detectable from Earth but that are at extreme enough viewing angles so as to generally be excluded from standard flare-forecasting methods (see discussions in Barnes et al., 2016; Leka et al., 2019a; Park et al., 2020). Far-side or invisible ARs (“Far”) are fully invisible from the Earth.

The latter boundary is not fixed; we establish whether or not a simple semi-circle of a size based on the half-width (in longitude) of the AFT-AR and centered at the region’s MCOM location, would extend beyond the visible limb. What is calculated first is essentially the minimum height that could be visible from the region’s Stonyhurst longitude θ_{Stony} :

$$h_{\min} = R_{\odot} \left(\frac{1}{\cos \theta_p} - 1.0 \right) \quad (5)$$

where $\theta_p = \theta_{\text{Stony}} - 90^\circ$ is the distance (in longitude degrees) beyond the limb. Then, if the semicircle that subtends the region’s size has $h > h_{\min}$, the region is denoted as “Occulted”, otherwise it is a fully invisible “Far” AR.

2.3.2 Magnetic Field Characterization

Throughout, only pixels greater than an estimate of the AFT-map noise are included in the analysis that produces the parameters. Based on the standard deviation in weak-signal areas this is around 15 Mx cm^{-2} , whereas the AFT-AR identification and tracking necessarily uses a higher threshold. Thus, only using pixels within the AFT-AR “blobs” (see Fig. 1) for the parametrization module ensures that we only use pixels within the AFT-AR delineation and thus significantly above the noise level.

As this is a “proof of concept”, we limit the number of magnetic field parameters that we present here to two, and use them together for multi-parameter analysis.

The first parameter is the total magnetic flux of the region. As discussed in Sawyer et al. (1986); Welsch et al. (2009); Barnes et al. (2016), the total magnetic flux is an extensive parameter (related to the AR’s size) that is well-known to be a fairly good predictor of flare activity and to some extent can act as a benchmark against which to compare more sophisticated analysis. As such, the total unsigned magnetic flux is simply $\Phi = \sum_{i=0}^N |B_{r,i}| A_i$ where $B_{r,i}$ is the radial magnetic flux density in each i^{th} pixel (Mx cm^{-2}) over the N pixels in the AFT-AR blob, and A_i is the pixel size in cm^2 .

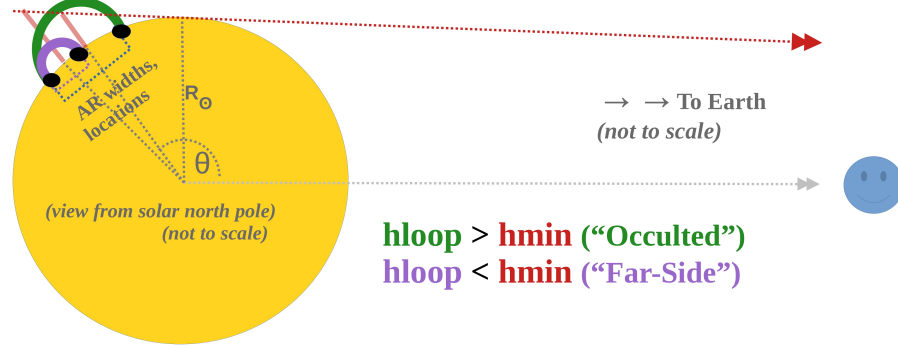


Figure 3. Cartoon representation (with absolutely no scale intended) of a far-side AR region (purple) and an occulted region (green), and the effective Stonyhurst longitude $\theta > 90^\circ$ indicated. For both loops, red line-segments indicate the minimum height that an AR loop system would need to achieve to be visible from Earth. As the cartoon indicates, our model that assesses whether an AR is to be labeled “Far-Side” or “Occulted” depends on the AR size and location.

A second parameter that is available from just the B_r distribution but which also performs well on large-sample evaluations is the \mathcal{R} parameter of Schrijver (2007), or the total magnetic flux in the immediate vicinity of strong-gradient polarity-inversion lines (SGPIL). The polarity inversion lines are identified using a method similar to that described in (Schrijver, 2007), essentially masking each polarity individually, growing these masks, and identifying where they overlap as the SGPIL. We use a 100 Mx cm^{-2} threshold and a 2-pixel ($\approx 8.5 \text{ Mm}$) width; additionally we erode and grow the resulting map to remove single-pixel areas, and finally extend the boundaries by ≈ 2 pixels. This final area is the vicinity of “strong-gradient PILs” (s), noting that (1) there may be more than a single SGPIL across a magnetic region, and that (2) we intentionally take a small area around it, since a PIL is by definition a width-less line. The specific values and thresholds used here differ from the original (Schrijver, 2007), but recover the intended morphology given the different data source, sensitivity, data grid, and spatial resolution. We then calculate the area of the AFT-AR that satisfies these criteria, and the flux contained within it.

It does happen that AFT-ARs will be centered close to the Carrington Longitude= $[0^\circ, 360^\circ]$ boundary. In this case, the analysis module identifies the situation, and creates a new map with the longitude “seam” at Longitude= 180° , wrapping the AFT-map and thus enabling the split region to be parameterized as a whole.

2.4 Statistical Approach for 4π Flare Forecasting

For this proof of concept study, we focus on statistical classification of labeled data. As mentioned above, fully validating on far-side flare activity is beyond the scope here; we focus on the ability to perform limb-flare region classification with, *vs.* without, relevant region information.

2.4.1 NWRA Classification Infrastructure

The statistical evaluations performed here deploy the NWRA Classification Infrastructure (NCI), which is the “research arm” of the operationally-running NWRA Dis-

criminent Analysis Flare Forecasting System (DAFFS; Leka et al., 2018). NCI is a well-established statistical classifier facility that has served, both in its present form and during its earlier development, as the statistical analysis tool for numerous investigations (Leka & Barnes, 2003; Barnes et al., 2007; Barnes & Leka, 2006; Leka & Barnes, 2007; Komm et al., 2011; Barnes et al., 2014; Welsch et al., 2009; Barnes et al., 2017; Lin et al., 2021; Leka et al., 2023). Based on nonparametric discriminant analysis (NPDA; Kendall et al., 1983), NCI uses non-parametric estimates of the probability density functions from samples of known populations to assign membership for a new measurement, with cross-validation. In its basic form, DA produces a categorical prediction. By using Bayes' theorem, this is extended to produce the probability that a measurement belongs to one of two (or more) populations: if \mathbf{x} belongs to population j , then

$$P_j(\mathbf{x}) = \frac{q_j f_j(\mathbf{x})}{q_1 f_1(\mathbf{x}) + q_2 f_2(\mathbf{x})}. \quad (6)$$

where q_j is the prior probability of belonging to population j , $f_j(\mathbf{x})$ is the probability density function for population j , and for this study $j = 2$ refers to the event population, while $j = 1$ refers to the non-event population.

From these density estimates and probabilities, NCI outputs a broad range of evaluation data and metrics to quantify the ability of the chosen input parameter(s) to discriminate between the populations (see Section 2.4.3). For the nature of this study, we are not invoking bootstrap estimates of the uncertainties at this juncture, but estimate skill-score uncertainties based on experience with similar sample sizes (Leka et al., 2018, 2023).

The needed components for NCI input are parameters to evaluate (Section 2.3), and the labels for those parameters which takes the form of an “event list” (Section 2.4.2). The NCI code package is designed to accommodate project-specific needs; in the present case, the relevant modules were modified as per the specifics of the AFT-map parameters in particular the visibility labels.

2.4.2 Event-List Generation

The event lists construct the labels for the samples to be evaluated by means of the nonparametric density estimates. What is needed for this project is the time and location of a flare start, and an eventual peak magnitude of that flare. The initial data source is the NOAA edited flare event lists (NOAA/Space Weather Prediction Center, 2024b), which reports flare parameters based primarily on the Geostationary Operational Environment System X-Ray Sensor (GOES/XRS; Garcia, 1994), in particular the 1–8Å Soft X-Ray sensor. For this study, we do not perform any further background subtraction or calibration.

The NOAA-provided flare lists do include some errors and missing information. In particular, a number of flares are un-matched to NOAA AR Numbers, or are missing location information. Missing information is especially common for flares that occur just behind the solar limb. We performed a curation of the dataset with particular attention to these events. A listed event for which a NOAA AR was assigned but a location was not, was confirmed and a location assigned using NOAA Region Lists and standard differential rotation rates, including propagating beyond-limb locations. Beyond-East-limb events are assigned to a “future-assigned” NOAA AR according to date, location, and backwards-propagating differential rotation. If there is no location or NOAA AR number, we manually searched for a coinciding event using numerous available resources including NOAA/SWPC H α flare event listings, Solar Monitor (Gallagher et al., 2002), the *SolarSoft* “Latest Events Archive” (Freeland & Handy, 1998; S. Freeland, 2025), and other on-line public resources. All assignments that involved such sleuthing are, of course, subject to interpretation; the curated list is available with the supporting data for this paper (Leka et al., 2025). Relevant for the analysis below, however, is a recognition that

Table 2. Region and Flare Sample Sizes 2010.06 – 2016.12

Sample Description	Region-by-Region On-Disk Regions	Occulted Regions
AFT-ARs (“HMI Baseline”)	23,485	4,825
C1.0+ flares	5,929	302
M1.0+ flares	1,012	67
AFT-ARs (“HMI + GONG ”)	23,892	6,580
C1.0+ flares	5,923	522
M1.0+ flares	1008	127
Sample Description	Full-Disk # Samples	#C1.0+ Flares/ # M1.0+ Flares
AFT-ARs (“HMI Baseline”)	6,911	3,895 / 950
AFT-ARs (“HMI + GONG ”)	6,944	3,995 / 1002

Earth-viewpoint detection of `Occ` flares will be necessarily undercounted due to attenuation effects.

Thus, the AFT-ARs are linked to the flare events through their association with the NOAA AR numbering, as described above. AFT-ARs may persist for multiple solar rotations, and therefore may be associated with more than one NOAA AR. Region and event matching was done via Carrington longitude and latitude, and by date. At this juncture, we are not attempting to incorporate truly far-side events as may be observed by, *e.g.*, the Spectrometer and Telescope for Imaging X-rays (STIX; Krucker et al. (2020); Xiao et al. (2023)) on board Solar Orbiter; such a large task is beyond the scope of this initial proof-of-concept study.

We generate lists based on two thresholds that defined an event, at the peak-flux levels of 10^{-6} W m^{-2} (C1.0) and 10^{-5} W m^{-2} (M1.0), with a validity period of 24 hr starting at 00:00, 08:00 and 16:00UT. The list associates an event (or lack of event) within the validity period for each AFT-AR. “Full-disk” event lists are then generated simply by tabulating whether any event occurred within any `Disk` or `Occ` AFT-AR. Of note, the AFT maps are sampled three times per day with 8 hr of evolution between each sample which we argue provides for derived parameters that are independent; the final relevant sample sizes are given in Table 2.

2.4.3 Validation Statistics

The NPDA produces a probability that a data point (from the parametrization) belonging to one of the assigned populations. In this case, we invoke two populations - flare-imminent and flare-quiet at the levels and in the validity periods described in Section 2.4.2. One evaluation metric reported here is the Brier Skill Score (essentially a Mean Square Error Skill Score) which summarizes Reliability Plots that graphically show a probabilistic classification’s reliability, skill, and resolution (see Barnes et al., 2016; Leka et al., 2019a, for discussion). The Reliability plots and BSS metric do not rely on setting a threshold (P_{th}) at which a probability becomes a “predict event” *vs.* “predict no-event”, in order to populate a “truth table” of True Positives, False negatives, *etc.*

We also produce Receiver (Relative) Operating Characteristic (Curve) (ROC) plots that compare the False Alarm Rate to the Probability of Detection, essentially the components of the “truth table” as the P_{th} is stepped between [0.0, 1.0]. The ROC Skill Score (ROCSS, see Leka et al. (2019a) for discussion) summarizes the ROC plot with a nor-

malized area under the curve such that ROCSS=0.0 corresponds to no skill, and ROCSS=1.0 is perfect skill. As such, the BSS and ROCSS provide comprehensive information without being sensitive to an assigned P_{th} .

The Peirce Skill Score (also known as the True Skill Statistic (TSS); Barnes et al. (2016); Bloomfield et al. (2012); Leka et al. (2019a)) is a dichotomous skill score popular in the literature. It has been shown to have a maximum when the probability threshold is equal to the event rate, or $P_{\text{th}} = R = N_{\text{event}}/N_{\text{total}}$ (Bloomfield et al., 2012; Kubo, 2019). The location of $\text{max}(\text{TSS})$ on the ROC curves is indicated; it is the location of the maximum vertical distance from the $x = y$ “no skill” line in the ROC plots. The $\text{max}(\text{TSS})$ scores here are all “reasonable” (ranging roughly 0.45 - 0.6) but at some level, TSS and other dichotomous skill scores are distracting due to their sensitivity to P_{th} .

In this investigation, the climatological rate is an interesting challenge due to the presumed attenuation of detected flares just beyond the solar limb (Woods et al., 2006), and the inability to accurately account for N_{total} . The event rate R for `Disk` is the most accurate since all information should be present and accounted for. Thus, all climatological event rates applied during evaluation are $P_{\text{th}} = R_{\text{Disk}}$.

Of interest here are the missed forecasts for events that could be Earth-impacting, *i.e.* the “False Negatives”, thus we include in our validation statistics the change in FN entries (“ ΔFN ”) between the test cases (`F11` *vs.* `F10` or `FH11` *vs.* `FH10`) when $P_{\text{th}} = R_{\text{Disk}}$. For completeness but without dwelling on results that are sensitivity to P_{th} , we also report the change in “False Positives” (false alarms) between the tests. Finally, we also report the number of `Occ` flares correctly predicted, or “True Positives”, when limb information is included (the `F11` and `FH11` tests), for comparison to zero (necessarily) when no information is present (the `F10` and `FH10` tests), again when $P_{\text{th}} = R_{\text{Disk}}$.

We refrain from reporting numerous other skill scores in detail, since for this study the emphasis is not on the performance of the classification itself (as long as it is reasonable, and not pathologic), but on evaluating improvements gained by having additional information beyond Earth-facing sources.

2.5 The Tests

Tests are designed to evaluate the “Delta”, or gain (if any) in the statistical classification performance enabled by the availability of near- and beyond-limb magnetic field data in the context of near- and beyond-limb flares. The different test configurations is given in Table 3, with boolean indicators as to whether the occulted regions are included in the density estimates (the “training”).

For the tests, all event lists were the same in terms of the flare events included, according to the threshold as indicated. In other words, if a flare occurred beyond the limb (but was detected in SXR by GOES), it was included as an ‘event’. It is extremely likely that the smaller flares from larger regions beyond the limb are under-sampled, presenting a bias. However, as the eventual goal of any flare forecasting approach is to forecast for impactful events, we use the GOES-based detection of the flares as a ground-truth in this study.

2.5.1 Disk Regions *vs.* Occulted Regions

The basic approach is to compare the NCI classification performance according to whether or not the occulted regions are included when “training” the system – *i.e.* computing the nonparametric density estimates upon which the region-based event probabilities are computed. The moniker indicates the boolean for [`Disk`,`Occ`] regions included, that is “10” *vs.* “11” in Table 3 indicate not including and including the `Occ` regions, respectively.

Table 3. Summary of Tests

Moniker	Disk Regions?	Occulted Regions?	Data / Region Input	Probability Basis
F10	Y	N	Surface Flux Transport only	Region-by-Region
F11	Y	Y	” ”	” ”
F10-FD	Y	N	” ”	Full-disk
F11-FD	Y	Y	” ”	” ”
FH10	Y	N	Surface Flux Transport + Helioseismology	Region-by-Region
FH11	Y	Y	” ”	” ”
FH10-FD	Y	N	” ”	Full-disk
FH11-FD	Y	Y	” ”	” ”

In other words, for all *10 tests, the region probabilities are computed using only the on-disk data and on-disk outcomes, duplicating the general approach of most forecasting facilities (see discussions in Barnes et al., 2016; Leka et al., 2019a, 2019b). In contrast, all *11 tests have region probabilities computed according to both the parameters (AFT-ARs) and outcomes, meaning on-disk (**Disk**) and occulted (**Occ**) parameters are used and both on-disk and occulted flares are used to compute the region probabilities.

For the evaluation, however, the event lists against which all *10, and *11 tests are evaluated include all detected and region-assigned flares. For the “10” tests, **Occ** AFT-ARs are assigned a probability of 0.0 throughout. In this test, then, any **Occ** flare would be registered necessarily as a “miss” although **Occ** non-event outcomes are registered as “true negatives”. This is not *exactly* the same as having “no information” that a region is present, however many systems would assign a climatological prediction to a region about which there is otherwise no quantitative information, which would be generally $\gg 0$ and thus in fact directly indicates some knowledge of a region’s existence. In the scheme adopted here, we are assured that occulted regions in the “10” tests will register a “miss” or False Negative, but there is a bias towards True Negatives.

2.5.2 *Surface Flux Transport Only vs. Surface Flux Transport + Helioseismology*

Tests are constructed to evaluate the additional performance enabled by incorporating far-side information from helioseismology (Table 3). These maps from which the parameters are calculated appear otherwise indistinguishable, but underlying them are either the “AFT-Baseline” AFT maps which assimilate data only from HMI into the flux transport (“F” monikers in Table 3), or the “AFT+GONG” maps that include AFT-ARs detected and tracked from the GONG helioseismic data (“FH” in Table 3; see Section 2.1).

As is expected, there are just over 2,000 additional data points (AFT-ARs at any given target time every 8 hr) over the 6.5-year period in the FH11 dataset over the F11, as the additional helioseismology information provides additional AR detections (Table 2). The impact of this additional information is clearly seen in the number of flare-positive AFT-AR data points, which are significantly more for the AFT+GONG than the AFT Baseline (for both C1.0+ and M1.0+) for the occulted areas **Occ**; the on-disk flare-positive AFT-AR data points are essentially equal, also as expected given the data assimilation.

2.5.3 Region-by-Region *vs.* Full Disk

The region-by-region tests compare directly the probability of an event being produced by a particular region with the outcome, as described above. The sample sizes are decently large and this is the manner by which many forecasting algorithms work. In practice, however, the location of the flare itself is irrelevant (unless it initiates a forecast for related phenomena such as energetic particles; Whitman et al., 2023). Additionally, full-disk forecasts can enable methodology comparisons when the definitions of an AR differ (Leka et al., 2019a).

Hence, we conduct tests using a “full-disk approach” (Leka et al., 2019a, Appendix B), meaning Sun-as-a-star-like, or agnostic of flare location of the originating AFT-ARs. The full-disk probabilities are constructed for each time from the AFT-AR probabilities (see Leka et al., 2019a):

$$P_{FD} = 1.0 - \prod (1.0 - P_{AFT_AR}) \quad (7)$$

where P_{AFT_AR} is each AFT-AR’s probability at a given time, and P_{FD} is the full-disk probability of an event. As with the region-by-region tests, the F10-FD and FH10-FD tests comprise probabilities for the on-disk AFT-ARs computed only against the on-disk events, and occulted AFT-ARs are assigned $P_{AFT_AR} = 0.0$ prior to computing the full-disk probabilities. In this manner, the occulted AFT-ARs do not add to the full-disk event probabilities for the F10-FD and FH10-FD tests. On the other hand, for both the F11-FD and FH11-FD tests, they do. For all -FD tests, the evaluation is performed using the full event list but (where applicable), $P_{th} = R_{Disk}$. As such, there are 33 additional full-disk samples in the GONG-supplemented AFT-maps that can be analyzed in the time-period because at least one “Occ” region is identified where none are present in the AFT Baseline maps.

While in practice some operational forecasting systems treat “no/missing data” or “bad data” by assigning a climatology-based forecast (Leka et al., 2018, 2019a) - in this case we strive to demonstrate the stringent scenario of the differences between having information *vs.* not. Such a treatment also provides the most interpretable results.

3 Results

The results presented here are in the spirit of a “proof of concept”. Little effort has been made to achieve the best possible performance, beyond deploying two parameters that have been shown to have relevance for solar flare productivity.

3.1 A Tale of Two Limb Flares

So, did it work? We look first at two examples, one a classification success and the other a classification failure.

3.1.1 Success: NOAA AR 12192 in October 2014

NOAA AR 12192 transited the disk mid-late October and displayed significant flare activity. The flares started before it was actually visible, however. On 2014.10.14 at 08:00 UT and then again at 16:00 UT, the probability of an M1.0+ flare using the AFT+GONG (FH-11) test was > 0.1 (significantly larger than the $R = 0.043$ climatology). At this point the AR was centered at -125° longitude, or 35° beyond the limb, but produced two GOES-detected M-class flares (M1.1 at 18:37 UT and M2.2 at 19:07 UT). The probabilities stayed high, and indeed, AR 12192 is a notable flare-active AR for Solar Cycle 24.

Table 4. Results Summary: Region-by-Region

Test	Event	Climato- logy (R)	$\Delta(FN)$ $P_{th}=R$	$\Delta(FP)$ $P_{th}=R$	TP (0cc) $P_{th}=R$	ROCSS	Δ ROCSS	BSS	Δ BSS
F10	C1.0+	0.252			0	0.606		0.255	
F11	” ”	” ”	-10	-1	116	0.617	+0.011	0.264	+0.009
F10	M1.0+	0.043			0	0.676		0.161	
F11	” ”	” ”	-26	+190	34	0.734	+0.058	0.178	+0.017
FH10	C1.0+	0.248			0	0.574		0.232	
FH11	” ”	” ”	+31	-9	155	0.584	+0.010	0.240	+0.008
FH10	M1.0+	0.042			0	0.615		0.149	
FH11	” ”	” ”	-24	-111	60	0.718	+0.103	0.151	+0.002

In contrast, the AFT-Baseline test that includes no far-side information had a probability of ≈ 0.01 for both of those 2014.10.14 times quoted above. The probabilities increased upon HMI data assimilation, but by that time the region had flared numerous times.

3.1.2 Failure: NOAA AR 12205 in November 2014

This particular AR grew and diminished repeatedly during its lifetime with varying flare productivity, according to multiple analysis efforts, and proved to be a significant challenge. A new GONG-identified AFT-AR appears in the AFT+GONG maps at the end of October 2014 (AFT-ID 20141027TN21014, *i.e.* emerging 2014.10.27 at N12 014 Carrington Longitude) at almost -180° Stonyhurst longitude. This AFT-AR then disappears on 2014.10.31 at 16:00 UT near $\approx -130^\circ$ Stonyhurst longitude. As this Carrington longitude rotates into view and the HMI data-assimilation begins, the magnetic flux concentrations grow starting 2014.11.05 and it acquires a new AFT-ID 20141108TN15010 – but then it again decreases in size a few days after that. As such, unfortunately, the large and loop-visible 0cc M-class flares on 2014.11.05 were classification misses. Finally, after 2014.11.06 (when the AFT-AR and now NOAA AR 12205 was at \approx E60 Stonyhurst and fully a Disk) AR, the subsequent multiple large flares were correctly classified.

Indeed an analysis using different approach (Hamada et al., 2024, 2025) corroborated that the seismic signature in this location diminished between 2014.10.27–2014.10.29. This particular AR may prove to be a good test-case for future improvements to helioseismic detection of near-limb ARs.

3.2 Large-sample Analysis

A summary of the full-sample tests and their resulting metrics are shown in Table 4 for region-by-region tests and in Table 5 for Full-Disk tests. ROC plots are shown in Figures 4 – 5, and Reliability plots are shown in Figures 6 – 9.

Overall the ROCSS and BSS are respectable on their own, and as has been stated before, are not the focus here. The BSS decrease with higher flare threshold (M+) whereas ROCSS increase, as has been seen previously (Barnes et al., 2016; Leka et al., 2019a). Both the ROC plots and Reliability plots on “on par” with those shown in numerous publications, confirming that the “ 4π -framework” is generally performing as expected.

Table 5. Results Summary: Full Disk

Test	Event Definition	Climatology (R)	$\Delta(\text{FN})$ $P_{\text{th}}=R$	$\Delta(\text{FP})$ $P_{\text{th}}=R$	$\text{TP}(\text{Occ})$ $P_{\text{th}}=R$	ROCSS	ΔROCSS	BSS	ΔBSS
F10-FD	C1.0+	0.446			0	0.719		0.383	
F11-FD	" "	" "	-73	+62	15	0.723	+0.004	0.394	+0.011
F10-FD	M1.0+	0.108			0	0.656		0.188	
F11-FD	" "	" "	-37	+85	0	0.686	+0.030	0.209	+0.021
FH10-FD	C1.0+	0.426			0	0.687		0.343	
FH11-FD	" "	" "	-90	+45	49	0.702	+0.015	0.364	+0.021
FH10-FD	M1.0+	0.103			0	0.627		0.174	
FH11-FD	" "	" "	-50	+15	4	0.662	+0.035	0.176	+0.002

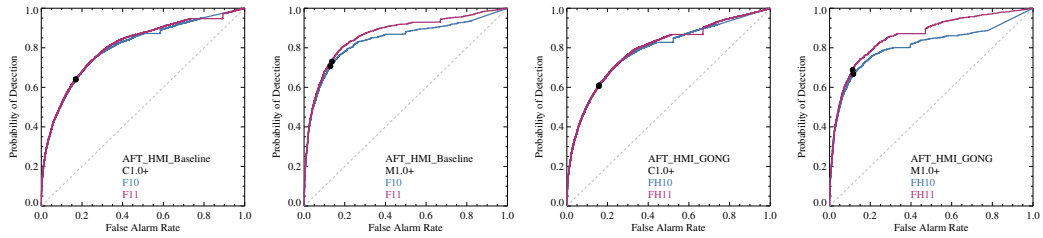


Figure 4. ROC plots for the region-based forecasts, comparing the paired tests as indicated (c.f. Table 3). For each, the P_{th} location on the ROC curve is indicated, where the TSS = POD-FAR is maximum, is indicated. The associated ROCSS and the differences between the paired tests are provided in Table 4.

The statistical improvements upon adding “Occ” data are overall in the ‘direction’ that is expected: ROCSS and BSS scores improve, although the magnitude by which they increase with additional information is not large, especially for the F-FD and FH-FD tests. We expect the region-based uncertainties in these skill scores to be $\simeq 0.01$ (C+) and $\simeq 0.02$ (M+) given the sample sizes (Barnes et al., 2016; Leka et al., 2018, 2023). As such, the improvements as seen by ΔROCSS are of order 1σ for C1.0+ and over 3σ for M1.0+, but all in the $\approx 0.0\sigma - 1.0\sigma$ range for ΔBSS .

These minor but positive improvement trends are reflected in the plots as well. The ROC plots for C1.0+ for F10 *vs.*, F11 and FH10 *vs.* FH11 tests show little difference, while there is a distinct difference for M1.0+ ROC plots (Figure 4) as less scatter between probability bins. The improvement is more noticeable for the FH test than the F, which is reflected in the higher ΔROCSS in Table 4. Any differences in the Reliability plots are difficult to gauge by eye – as reflected in the ΔBSS . For FH-11 / M1.0+, one can see a slight improvement as a “tightening” around the $x = y$ line for lower-probability bins, but a distinct over-forecasting especially at higher probabilities that is somewhat more pronounced than for the FH-10 test. This trend is directly related to the under-representation of Occ flares, meaning it is more an under-detection than an over-forecast.

The full-disk tests (F-FD and FH-FD) show similar statistical results: all $\Delta[\text{ROCSS}, \text{BSS}]$ are in the correct “direction”, but the statistical improvements are small. This result is not unexpected given the overall small fraction of ARs and flares that reside in the “Occ” regime.

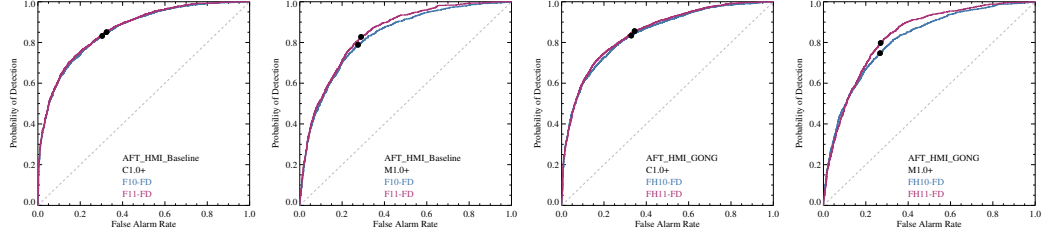


Figure 5. Same as Figure 4 but for full-disk forecasts, with associated ROCSS given in Table 5.

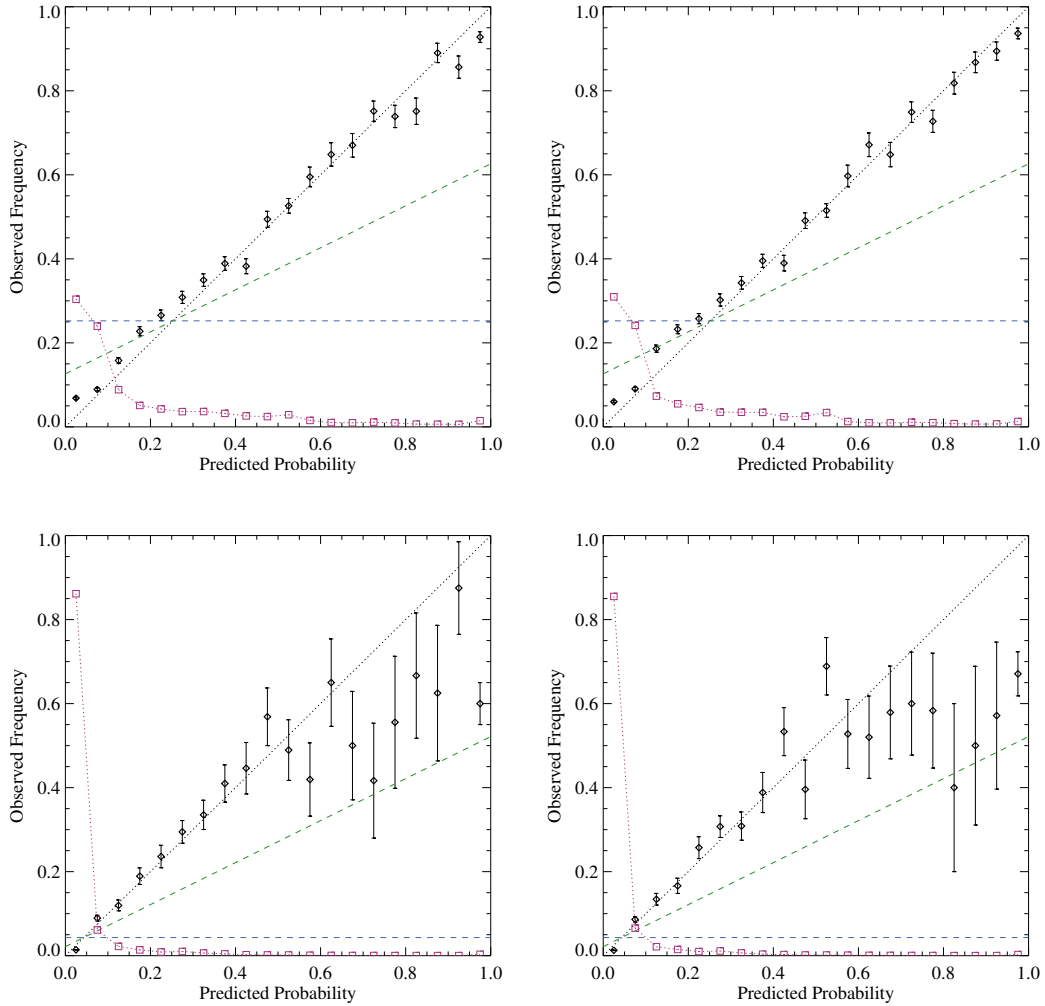


Figure 6. Reliability Plots for the AFT-HMI Baseline data without (F10, left) and with (F11, right), the occulted-region data included, for C1.0+ flares (top) and M1.0+ flare (bottom). The predicted probabilities are divided into 20 bins, and the error bars reflect the sample size of that bin (Wheatland, 2005). Also shown are the sample-size histograms (red), the climatology (blue) and the “no-skill” line (green).

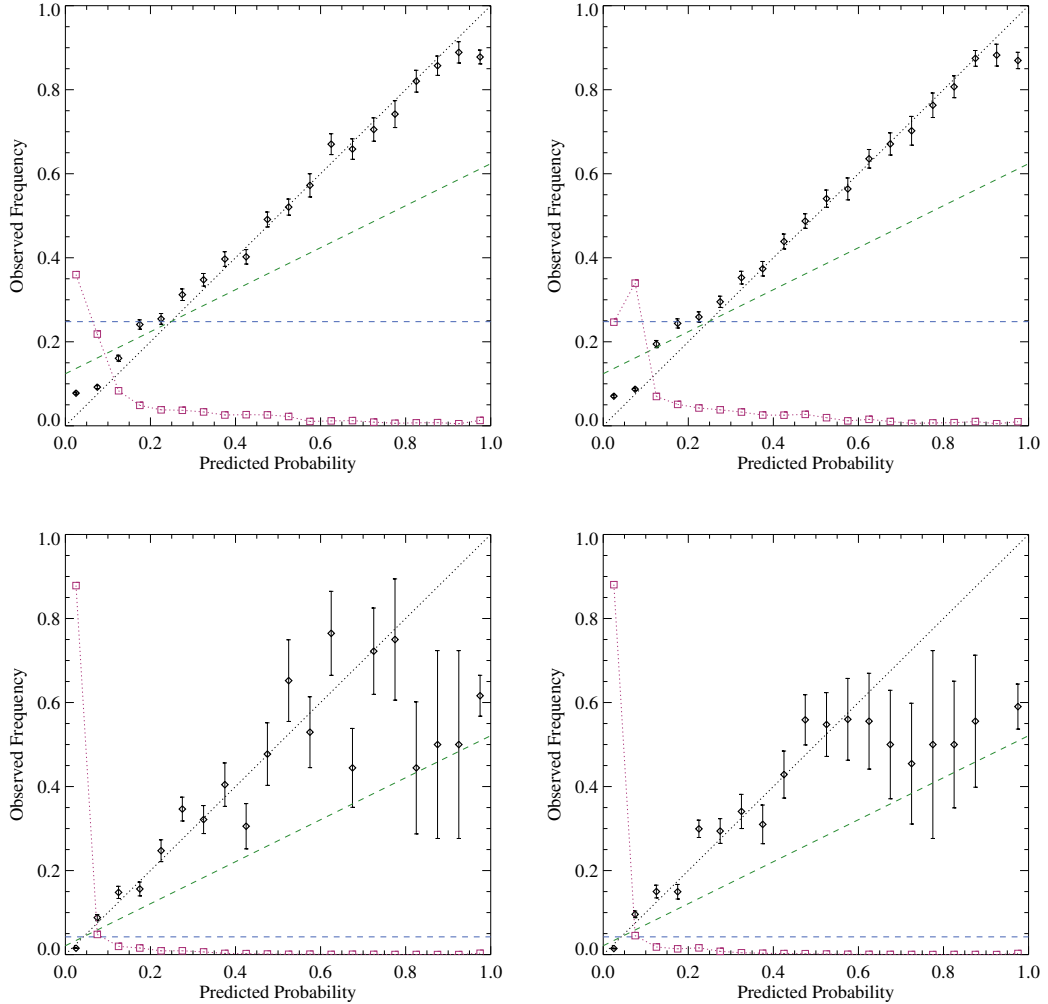


Figure 7. Same as Figure 6 but for the AFT-maps informed by the GONG-based helioseismology, *i.e.* FH10 (left) and FH11 (right).

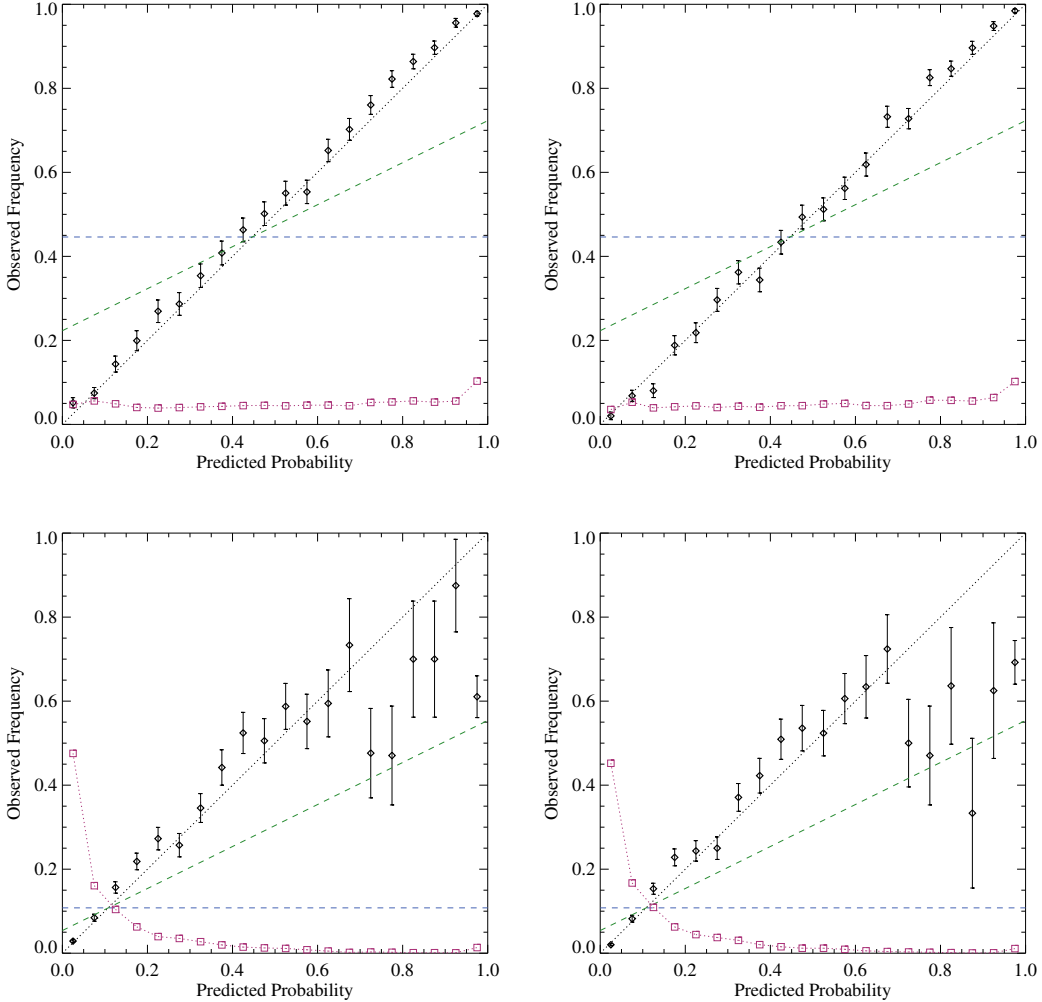


Figure 8. Same as Figure 6 but for Full-Disk forecasts, *i.e.* F10-FD (left) and F11-FD (right).

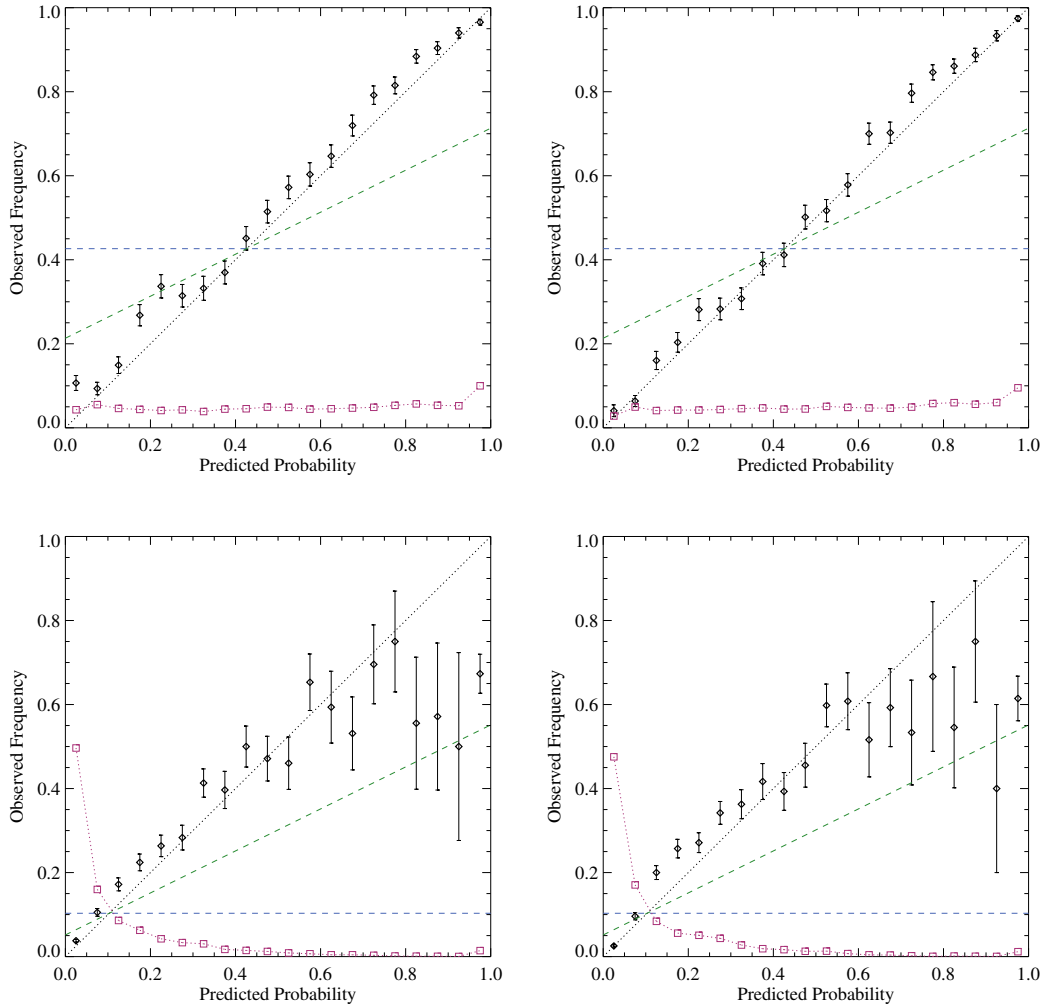


Figure 9. Same as Figure 7 but for Full-Disk forecasts, *i.e.* FH10-FD (left) and FH11-FD (right).

Table 6. East *vs* West “0cc” Success (Region-by-Region)

Test	Event Def.	Climatology	N_{East}	N_{West}	Imbalance (H)
F11	C1.0+	0.252	8	108	0.86
FH11	C1.0+	0.248	45	110	0.42
F11	M1.0+	0.043	2	32	0.88
FH11	M1.0+	0.042	24	36	0.20

The ROC plots for the FD-tests are again minimally improved for C1.0+, noticeably improved (albeit a small improvement) for M1.0+, with the FH test showing a larger visual improvement. It is difficult to see trends in the Reliability plots, as expected from the ΔBSS results, except for an improvement for the lower-probability bins in the FH11-FD compared with the FH10-FD for C1.0+.

Both region-based and full-disk-based tests generally show reductions in False Negatives, more significantly for the F-FD and FH-FD tests and except for the FH (region) case. The trend is encouraging, although the specific numbers are sensitive to P_{th} and the difference between P_{th} for Disk and Disk+0cc can be up to 25% from the available event lists again due to the under-detection of events for 0cc plus the unknown “non-event” rate. There are generally trade-offs within a truth-table between False Negatives and False Positives and this is seen in Tables 4, 5. Depending on user preferences, $P_{\text{th}} = R_{\text{Disk}}$ indeed the False Positives may or may not decrease with the added 0cc-data information.

With those P_{th} caveats in mind, most telling are the “TP (0cc)” entries. For all “-10” tests these are necessarily “0”, meaning that no 0cc event is successfully classified. For all but one of the “-11” tests, TP(0cc) $\gg 0$ showing that with the 4π information, near-, at-, and just-beyond-limb events were indeed successfully classified. For the FD tests, the numbers are smaller than region-tests, but one must remember that these represent essentially 4π evaluations from the Earth vantage point: each TP (0cc) entry represents a 24 hr period (recalling our 8 hr sampling) when the *only* event was a 0cc event, and that without the 4π information provided, that event would have been missed. Moreover, the AFT-GONG FH tests provide systematically more such cases than AFT-Baseline for both region- and FD-based tests, demonstrating that the additional information provided by the far-side helioseismology can lead to better limb-ward flare classification.

The difference between East- and West-limb 0cc classification performance can be used to test the hypothesis that better outcomes are expected for the West-limb flares due to data being more recently-assimilated into the AFT model. We present in Table 6 the results of the correctly-classified 0cc AFT-ARs separated by East-limb *vs.* West-limb. The number of correct classifications uses the same $P_{\text{th}} = R_{\text{Disk}}$ as in Table 4, and the “Imbalance Ratio” follows the Flux Balance (Eqn. 2), $H = |(N_{\text{East}} - N_{\text{West}})| / N_{\text{total}}$ so that $H = 0$ is perfectly balanced and $H = 1$ is perfectly imbalanced with $N_{\text{East}}, N_{\text{West}}$ being the true positives for East- and West-limbs respectively. This hemisphere-focused analysis confirms the stated hypothesis when solely the AFT model is used (the F11 tests), by way of high imbalance ratio and a dominance by N_{West} . Importantly, the imbalance ratio significantly decreases when the far-side seismology information is included (the FH11 tests). It is clearly demonstrated thus, that the 4π framework improves limb-flare classification, and that there is significant value-added particularly for East-limb flares by including information provided by far-side helioseismology.

4 Discussion and Conclusions

We present here a proof-of-concept “ 4π Solar Energetic Event Forecasting System”, beginning with solar flares. In particular, we present this infrastructure looking forward to the need for full-heliosphere space-weather forecasts as more missions populate the solar system beyond the immediate Sun-Earth line. For the near-term we focus on the prospect of improving forecasts for Earth-impacting solar flares that occur near or just beyond the solar limb (the “Limb-Flare Challenge”) where the data usually relied upon to make these forecasts becomes unreliable or simply unavailable.

The new 4π framework consists of a surface flux transport model, information input from far-side helioseismology, and a statistical classifier. Additional components developed for this system include an appropriate flare event list (in this case, curated especially to characterize near- and beyond-limb flares), a new AR-identification and labeling scheme that mitigates problems brought by Earth-side sequential numbering schemes, and a validation methodology that evaluates performance statistically in the context of known detection bias present for this challenge.

Tests were performed for a statistically-significant sample size covering 6.5 years (numerous solar rotations), for both region-by-region and full-disk representations, following standard flare-forecasting event definitions. Even with this multi-year dataset, however, the sample sizes were not large, which meant that the differences between including the limb information and not could be statistically subtle. We mitigated this challenge somewhat by using overlapping validity periods (deploying 24 hr validity periods every 8 hr) to increase the sample size. Our argument, that the evolution of the AFT maps between 8 hr samples provides independent observation-classification outcome pairs, may not completely guard against bias due to non-independent event labels. We have tested the analysis using the data for the three times chosen separately (*e.g.*, three different sets of single-time sampling and 24 hr validity periods thus providing three sets of fully independent 24 hr labels and outcomes), each of which having roughly 1/3 the sample size of the “combined-data”. We have confirmed that for the present experiments, the 8 hr sub-sampling results in no significant bias being introduced to the probability distributions and that there are no statistically significant differences in the event rates or resulting skill scores, especially given the increased uncertainties expected from the smaller sample sizes. The primary differences seen between single-time results and the combined-data results are slightly improved skill scores for the latter due to the larger sample sizes and thus better determination of the probability density functions. The data by which to confirm our conclusions are available in the associated open-data repositories (Leka et al., 2025).

As such, our experiments find that information provided from solely the surface magnetic flux transport model can, indeed, improve the forecasts of Earth-visible limb flares according to standard validation metrics. In particular, this framework can reduce the number of “missed” events overall, and provide successful classification of West-limb-flares specifically. We find further improvement, in particular for East-limb flares, when far-side detection of new solar ARs or the growth of previously-identified regions are incorporated into the model using far-side helioseismology.

Arguably, the improvements we show are statistically small when evaluated over all visible flares. However, they are consistently in the expected direction, and demonstrate well this proof of concept. Every single piece of the process described here can be improved. Similarly, for each component of the framework a different methodology or data source could be invoked. We focus here on using data that are ostensibly available in an operational manner, meaning we do not need to rely on data from *off* the Sun-Earth line.

However, the new infrastructure presented here is notable, including:

1. a novel AR numbering scheme that avoids Earth-centric confusion brought on by solar rotation, allows for post-facto changes and provides unique identifiers;
2. methodology to incorporate the detection of far-side ARs and an evaluation of their magnetic properties, into a surface magnetic flux-transport model of the 4π Sun;
3. characterizing the 4π Sun using magnetic-field parameters known to be relevant to solar flare production;
4. developing the validation methodology for near-limb and occulted regions that are otherwise missed by the vast majority of flare-forecasting systems.

When or if it becomes timely to pursue an operational version of a 4π energetic-event forecasting tool, identifying the best-performing magnetic flux-transport system, most sensitive seismic detection algorithm, the most stable AR identification and tracking system, and the optimal set of magnetic parameters should indeed all be considered. Indeed, to achieve the best “limb-flare” predictions, one could consider combining this 4π magnetic field based approach with one that focuses on UV coronal emission visible above the solar limb (Leka et al., 2023; Lee et al., 2024). However, for this proof of concept, the point is not to obtain the highest possible skill scores. Instead we present a novel approach, describe the needed infrastructure that was developed, and demonstrate the utility of 4π “Full Heliosphere” space-weather forecasting by initially addressing the “Limb-Flare Challenge” failure-mode in today’s operational solar flare prediction.

Open Research Section

This project comprises data and code from many different sources, some “pipeline” and/or public, and some created specifically for this work. Listed roughly by the institution that provided the data and/or is the responsible party, the availability is as follows.

NSO:

1. Phase-shift maps are available at: <https://gong2.nso.edu/archive/patch.pl?menutype=farside#step2>

SwRI:

1. Baseline AFT maps are available, see Jha and Upton (2024). The most updated AFT Baseline map can be also obtained from https://data.boulder.swri.edu/lisa/AFT_Baseline/, which is being updated daily with latest available HMI magnetogram data.
2. AFT maps with GONG-informed input are available, see Jha, Upton, et al. (2025).
3. The AFT-AR code with which the AFT-ARs are identified, tracked, and labeled is available, see Jha, Sreedevi, et al. (2025)

NWRA:

1. A project-specific repository has been created, see Leka et al. (2025). In this repository we provide: IDL “save” files that include the AFT-AR parametrization data, and the event populations. These files contain summaries, essentially, of hundreds of output files otherwise produced that are large and contain significant amounts of data extraneous to this project. The forecast, or classifier probabilities are provided for each of the tests, and JSON files that summarize the AFT-ARs (provided by SwRI) are also provided here. Also provided are the “curated” event lists (the information from which informs the “POP” label in the IDL save files” structures).

2. NCI, by which probabilities are computed, is described in Leka et al. (2018). The linear version of discriminant analysis is available at <https://www.cora.nwra.com/~graham/DA.html>. Some project-specific compute-environment-specific data handling wrappers were developed and not included, as not being general analysis tools.
3. The codes for computing skill scores, ROCSS, and that are needed to produce the plots are provided in the (Leka et al., 2025) repository.

Acknowledgments

This project was funded primarily by NASA/R2O2R grant #80NSSC22K0273 with additional support from NASA LWS/SC grant 80NSSC22K0892 (subaward to NWRA); KJ was partially supported by the NSF Windows on the Universe - Multi-Messenger Astrophysics (WoU-MMA) grant to the National Solar Observatory. All opinions expressed herein are solely those of the authors. This work utilizes GONG data obtained by the NSO Integrated Synoptic Program, managed by the National Solar Observatory, which is operated by the Association of Universities for Research in Astronomy (AURA), Inc. under a cooperative agreement with the National Science Foundation and with a contribution from the National Oceanic and Atmospheric Administration. The GONG network of instruments is hosted by the Big Bear Solar Observatory, High Altitude Observatory, Learmonth Solar Observatory, Udaipur Solar Observatory, Instituto de Astrofísica de Canarias, and Cerro Tololo Inter-American Observatory. We acknowledge the HMI and SDO facilities and teams, as well as the GONG facility and team, especially Mitch Creelman, for making this project possible, Dr. Amr Hamada for input on NOAA AR 12205, and Dr. Graham Barnes for support on NCI. The authors also thank the two thoughtful referees who helped us clarify and strengthen the presentation.

Conflict of Interest Statement

The authors affirm there are no conflicts of interest.

References

Arge, C. N., Luhmann, J. G., Odstrcil, D., Schrijver, C. J., & Li, Y. (2004, October). Stream structure and coronal sources of the solar wind during the May 12th, 1997 CME. *Journal of Atmospheric and Solar-Terrestrial Physics*, *66*(15-16), 1295-1309. doi: 10.1016/j.jastp.2004.03.018

AstroPy Developers. (2025). *Sigma_clip*. https://docs.astropy.org/en/stable/api/astropy.stats.sigma_clip.html. (Accessed: 2024-2025)

Barnes, G., Birch, A. C., Leka, K. D., & Braun, D. C. (2014, May). Helioseismology of Pre-Emerging Active Regions. III. Statistical Analysis. *Astrophys. J.*, *786*, 19. doi: 10.1088/0004-637X/786/1/19

Barnes, G., & Leka, K. D. (2006). Photospheric Magnetic Field Properties of Flaring vs. Flare-Quiet Active Regions III: Magnetic Charge Topology Models. *Astrophys. J.*, *646*, 1303-1318. doi: 10.1086/504960

Barnes, G., Leka, K. D., Schrijver, C. J., Colak, T., Qahwaji, R., Ashamari, O. W., ... Wagner, E. L. (2016, October). A Comparison of Flare Forecasting Methods, I: Results from the 'All-Clear' Workshop. *Astrophys. J.*, *829*, 89. doi: 10.3847/0004-637X/829/2/89

Barnes, G., Leka, K. D., Schumer, E. A., & Della-Rose, D. J. (2007). Probabilistic Forecasting of Solar Flares from Vector Magnetogram Data. *Space Weather*, *5*, 9002. doi: 10.1029/2007SW000317

Barnes, G., Schanche, N., Leka, K. D., Aggarwal, A., & Reeves, K. (2017, June). A comparison of classifiers for solar energetic events. In M. Bresciani (Ed.), *Astroinformatics* (Vol. 325, p. 201-204). doi: 10.1017/S1743921316012758

Bloomfield, D. S., Higgins, P. A., McAteer, R. T. J., & Gallagher, P. T. (2012, March). Toward Reliable Benchmarking of Solar Flare Forecasting Methods. *Astrophys. J. Letters*, *747*, L41. doi: 10.1088/2041-8205

Bobra, M. G., Sun, X., Hoeksema, J. T., Turmon, M., Liu, Y., Hayashi, K., ... Leka, K. D. (2014, September). The Helioseismic and Magnetic Imager (HMI) Vector Magnetic Field Pipeline: SHARPs - Space-Weather HMI Active Region Patches. *Solar Phys.*, *289*, 3549-3578. doi: 10.1007/s11207-014-0529-3

Braun, D. C., & Lindsey, C. (2001, October). Seismic Imaging of the Far Hemisphere of the Sun. *Astrophys. J. Letters*, *560*(2), L189-L192. doi: 10.1086/324323

Centeno, R., Schou, J., Hayashi, K., Norton, A., Hoeksema, J. T., Liu, Y., ... Barnes, G. (2014, September). The Helioseismic and Magnetic Imager (HMI) Vector Magnetic Field Pipeline: Optimization of the Spectral Line Inversion Code. *Solar Phys.*, *289*, 3531-3547. doi: 10.1007/s11207-014-0497-7

Couvidat, S., Schou, J., Shine, R. A., Bush, R. I., Miles, J. W., Scherrer, P. H., & Rairden, R. L. (2012, January). Wavelength Dependence of the Helioseismic and Magnetic Imager (HMI) Instrument onboard the Solar Dynamics Observatory (SDO). *Solar Phys.*, *275*, 285-325. doi: 10.1007/s11207-011-9723-8

Freeland, S. (2025). *Solarsoft latest event*. https://www.lmsal.com/solarsoft/latest_events_archive.html. (Accessed: 2023 - 2025)

Freeland, S. L., & Handy, B. N. (1998, October). Data Analysis with the SolarSoft System. *Solar Phys.*, *182*(2), 497-500. doi: 10.1023/A:1005038224881

Gallagher, P. T., Moon, Y. J., & Wang, H. (2002, September). Active-Region Monitoring and Flare Forecasting I. Data Processing and First Results. *Solar Phys.*, *209*(1), 171-183. (see <https://solarmonitor.org>) doi: 10.1023/A:1020950221179

Garcia, H. A. (1994, October). Temperature and emission measure from GOES soft X-ray measurements. *Solar Phys.*, *154*, 275-308. doi: 10.1007/BF00681100

Georgoulis, M. K., Bloomfield, D. S., Piana, M., Massone, A. M., Soldati, M., Gallagher, P. T., ... Worsfold, M. (2021, May). The flare likelihood and region eruption forecasting (FLARECAST) project: flare forecasting in the big data

& machine learning era. *Journal of Space Weather and Space Climate*, 11, 39. doi: 10.1051/swsc/2021023

González Hernández, I., Díaz Alfaro, M., Jain, K., Tobiska, W. K., Braun, D. C., Hill, F., & Pérez Hernández, F. (2014, February). A Full-Sun Magnetic Index from Helioseismology Inferences. *Solar Phys.*, 289(2), 503-514. doi: 10.1007/s11207-013-0339-z

González Hernández, I., Hill, F., & Lindsey, C. (2007, November). Calibration of Seismic Signatures of Active Regions on the Far Side of the Sun. *Astrophys. J.*, 669(2), 1382-1389. doi: 10.1086/521592

González Hernández, I., Hill, F., Scherrer, P. H., Lindsey, C., & Braun, D. C. (2010, June). On the success rate of the farside seismic imaging of active regions. *Space Weather*, 8(6), 06002. doi: 10.1029/2009SW000560

Hale, G. E., Ellerman, F., Nicholson, S. B., & Joy, A. H. (1919, April). The Magnetic Polarity of Sun-Spots. *apj*, 49, 153. doi: 10.1086/142452

Hamada, A., Creelman, M., Jain, K., & Lindsey, C. (2025, June). FArSide Trained Active Region Recognition (FASTARR): A Machine Learning Approach. *Astrophys. J. Supp. Ser.*, 278(2), 53. doi: 10.3847/1538-4365/add893

Hamada, A., Jain, K., Lindsey, C., Creelman, M., & Oien, N. (2024, December). Far-side Active Regions Based on Helioseismic and EUV Measurements: A New Data Set for Heliospheric Machine Learning Advancements. *Astrophys. J.*, 977(1), 85. doi: 10.3847/1538-4357/ad8636

Harvey, J. W., Hill, F., Hubbard, R. P., Kennedy, J. R., Leibacher, J. W., Pin-tar, J. A., ... Yasukawa, E. (1996, May). The Global Oscillation Network Group (GONG) Project. *Science*, 272(5266), 1284-1286. doi: 10.1126/science.272.5266.1284

Hathaway, D. H. (2011, October). A Standard Law for the Equatorward Drift of the Sunspot Zones. *Solar Phys.*, 273(1), 221-230. doi: 10.1007/s11207-011-9837-z

Hathaway, D. H., & Upton, L. A. (2016, November). Predicting the amplitude and hemispheric asymmetry of solar cycle 25 with surface flux transport. *Journal of Geophysical Research (Space Physics)*, 121(11), 10,744-10,753. doi: 10.1002/2016JA023190

Hoeksema, J. T., Liu, Y., Hayashi, K., Sun, X., Schou, J., Couvidat, S., ... Turmon, M. (2014, September). The Helioseismic and Magnetic Imager (HMI) Vector Magnetic Field Pipeline: Overview and Performance. *Solar Phys.*, 289, 3483-3530. doi: 10.1007/s11207-014-0516-8

Jain, K., Tripathy, S. C., Hill, F., & Pevtsov, A. A. (2021, October). Continuous Solar Observations from the Ground-Assessing Duty Cycle from GONG Observations. *Pub. Astron. Soc. Pacific*, 133(1028), 105001. doi: 10.1088/1538-3873/ac24d5

Jha, B. K., Priyadarshi, A., Mandal, S., Chatterjee, S., & Banerjee, D. (2021, January). Measurements of Solar Differential Rotation Using the Century Long Kodaikanal Sunspot Data. *Solar Physics*, 296(1), 25. doi: 10.1007/s11207-021-01767-8

Jha, B. K., Sreedevi, A. B., Karak, B. B., & Banerjee, D. (2025, June). *autotabpy*. Zenodo. doi: 10.5281/zenodo.15666357

Jha, B. K., & Upton, L. (2024). *HMI AFT Baseline Maps*. Harvard Dataverse. doi: 10.7910/DVN/CGFKRE

Jha, B. K., Upton, L., Leka, K. D., & Jain, K. (2025). *AFT HMI+GONG Far-side Photospheric Radial Magnetic Field Map*. Harvard Dataverse. doi: 10.7910/DVN/AJ3LPD

Kendall, M., Stuart, A., & Ord, J. K. (1983). *The advanced theory of statistics* (4th ed., Vol. 3). New York: Macmillan Publishing Co., Inc.

Komm, R., Ferguson, R., Hill, F., Barnes, G., & Leka, K. D. (2011, February). Subsurface Vorticity of Flaring versus Flare-Quiet Active Regions. *Solar Phys.*, 268, 389-406. doi: 10.1007/s11207-010-9552-1

Krucker, S., Hurford, G. J., Grimm, O., Kögl, S., Gröbelbauer, H. P., Etesi, L., ...

Lin, R. P. (2020, October). The Spectrometer/Telescope for Imaging X-rays (STIX). *Astronomy and Astrophys.*, 642, A15. doi: 10.1051/0004-6361/201937362

Kubo, Y. (2019, April). Why do some probabilistic forecasts lack reliability? *Journal of Space Weather and Space Climate*, 9, A17. doi: 10.1051/swsc/2019016

Lee, J., Moon, Y.-J., Jeong, H.-J., Yi, K., & Lee, H. (2024, August). Can Solar Limb Flare Prediction Be Properly Made by Extreme-ultraviolet Intensities? *Astrophys. J. Letters*, 971(2), L47. doi: 10.3847/2041-8213/ad6b9b

Leka, K. D., & Barnes, G. (2003). Photospheric Magnetic Field Properties of Flaring vs. Flare-Quiet Active Regions II: Discriminant Analysis. *Astrophys. J.*, 595, 1296–1306.

Leka, K. D., & Barnes, G. (2007). Photospheric Magnetic Field Properties of Flaring vs. Flare-Quiet Active Regions. IV: A Statistically Significant Sample. *Astrophys. J.*, 656, 1173–1186. doi: 10.1086/510282

Leka, K. D., & Barnes, G. (2017). Solar Flare Forecasting: Present Methods and Challenges. In Buzulukova, N. (Ed.), *Extreme Events in Geospace: Origins, Predictability, Consequences* (First ed., chap. 3). Cambridge, MA, USA: Elsevier.

Leka, K. D., Barnes, G., & Wagner, E. L. (2017, February). Evaluating (and Improving) Estimates of the Solar Radial Magnetic Field Component from Line-of-Sight Magnetograms. *Solar Phys.*, 292, 36. doi: 10.1007/s11207-017-1057-8

Leka, K. D., Barnes, G., & Wagner, E. L. (2018, April). The NWRA Classification Infrastructure: Description and Extension to the Discriminant Analysis Flare Forecasting System (DAFFS). *Journal of Space Weather and Space Climate*, 8(27), A25. doi: 10.1051/swsc/2018004

Leka, K. D., Dissauer, K., Barnes, G., & Wagner, E. L. (2023, January). Properties of Flare-Imminent versus Flare-Quiet Active Regions from the Chromosphere through the Corona II: NonParametric Discriminant Analysis Results from the NWRA Classification Infrastructure (NCI). *Astrophys. J.*, 942, 84. doi: 10.3847/1538-4357/ac9c04

Leka, K. D., Park, S. H., Kusano, K., Andries, J., Balch, C., Barnes, G., ...

Terkildsen, M. (2019a, Aug). A Comparison of Flare Forecasting Methods. II. Benchmarks, Metrics and Performance Results for Operational Solar Flare Forecasting Systems. *Astrophys. J. Supp. Ser.*, 243(2), 36. Retrieved from <https://doi.org/10.3847/1538-4365/ab2e12> doi: 10.3847/1538-4365/ab2e12

Leka, K. D., Park, S. H., Kusano, K., Andries, J., Balch, C., Barnes, G., ... Terkildsen, M. (2019b, Aug). A Comparison of Flare Forecasting Methods. III. Systematic Behaviors of Operational Solar Flare Forecasting Systems. *Astrophys. J.*, 881(2), 101. Retrieved from <https://doi.org/10.3847/1538-4357/ab2e11> doi: 10.3847/1538-4357/ab2e11

Leka, K. D., Wagner, E. L., Petty, S., & Jha, B. K. (2025). *Replication Data for: “Addressing Known Challenges in Solar Flare Forecasting I: Limb-Flare Prediction with a 4π Full-Heliosphere Framework*. Harvard Dataverse. Retrieved from <https://doi.org/10.7910/DVN/3QQ5CO> doi: 10.7910/DVN/3QQ5CO

Lin, P. H., Kusano, K., & Leka, K. D. (2021, June). Eruptivity in Solar Flares: The Challenges of Magnetic Flux Ropes. *Astrophys. J.*, 913(2), 124. doi: 10.3847/1538-4357/abf3c1

Lindsey, C., & Braun, D. C. (2000, March). Seismic Images of the Far Side of the Sun. *Science*, 287(5459), 1799–1801. doi: 10.1126/science.287.5459.1799

MacDonald, G. A., Henney, C. J., Díaz Alfaro, M., González Hernández, I., Arge, C. N., Lindsey, C., & McAteer, R. T. J. (2015, July). Active Region Morphologies Selected from Near-side Helioseismic Data. *Astrophys. J.*, 807(1), 21. doi: 10.1088/0004-637X/807/1/21

Mosher, J. (1977). *The Magnetic History of Solar Active Regions* (Ph.D. Dissertation, California Institute of Technology, Pasadena, CA). (Defense date: 01 November 1976) doi: 10.7907/ZPPR-4490

NOAA/Space Weather Prediction Center. (2024a, Sept.). *R3 (Strong) HF Radio Blackout Observed*. <https://www.swpc.noaa.gov/news/r3-strong-hf-radio-blackout-observed>.

NOAA/Space Weather Prediction Center. (2024b). *Solar and Geophysical Event Reports*. <https://www.swpc.noaa.gov/products/solar-and-geophysical-event-reports>.

Odstrcil, D., Riley, P., & Zhao, X. P. (2004, February). Numerical simulation of the 12 May 1997 interplanetary CME event. *Journal of Geophysical Research (Space Physics)*, 109(A2), A02116. doi: 10.1029/2003JA010135

Park, S. H., Leka, K. D., Kusano, K., Andries, J., Balch, C., Barnes, G., ... Terkildsen, M. (2020, feb). A Comparison of Flare Forecasting Methods, IV: Evaluating Consecutive-Day Forecasting Patterns. *Astrophys. J.*, 890(2), 124. Retrieved from <https://doi.org/10.3847/2F1538-4357%2Fab65f0> doi: 10.3847/1538-4357/ab65f0

Pesnell, W. D., Thompson, B. J., & Chamberlin, P. C. (2012, January). The Solar Dynamics Observatory (SDO). *Solar Phys.*, 275, 3–15. doi: 10.1007/s11207-011-9841-3

Sawyer, C., Warwick, J. W., & Dennett, J. T. (1986). *Solar Flare Prediction*. Boulder, CO: Colorado Associated University Press.

Scherrer, P. H., Schou, J., Bush, R. I., Kosovichev, A. G., Bogart, R. S., Hoeksema, J. T., ... Tomczyk, S. (2012, January). The Helioseismic and Magnetic Imager (HMI) Investigation for the Solar Dynamics Observatory (SDO). *Solar Phys.*, 275, 207–227. doi: 10.1007/s11207-011-9834-2

Schou, J., Scherrer, P. H., Bush, R. I., Wachter, R., Couvidat, S., Rabello-Soares, M. C., ... Tomczyk, S. (2012, January). Design and Ground Calibration of the Helioseismic and Magnetic Imager (HMI) Instrument on the Solar Dynamics Observatory (SDO). *Solar Phys.*, 275, 229–259. doi: 10.1007/s11207-011-9842-2

Schrijver, C. J. (2007, February). A Characteristic Magnetic Field Pattern Associated with All Major Solar Flares and Its Use in Flare Forecasting. *Astrophys. J. Letters*, 655, L117–L120. doi: 10.1086/511857

Sheeley, N. R., Jr. (1966, May). Measurements of Solar Magnetic Fields. *Astrophys. J.*, 144, 723. doi: 10.1086/148651

Sreedevi, A., Jha, B. K., Karak, B. B., & Banerjee, D. (2023, October). AutoTAB: Automatic Tracking Algorithm for Bipolar Magnetic Regions. *The Astrophysical Journal Supplement Series*, 268(2), 58. Retrieved 2025-03-07, from <https://dx.doi.org/10.3847/1538-4365/acec47> (Publisher: The American Astronomical Society) doi: 10.3847/1538-4365/acec47

Sun, D., Huang, X., Zhao, Z., & Xu, L. (2023, May). Deep Learning-based Solar Flare Forecasting Model. III. Extracting Precursors from EUV Images. *Astrophys. J. Supp. Ser.*, 266(1), 8. doi: 10.3847/1538-4365/acc248

Svalgaard, L., Duvall, T. L., Jr., & Scherrer, P. H. (1978, July). The Strength of the Sun's Polar Fields. *Solar Phys.*, 58, 225. doi: 10.1007/BF00157268

Upton, L., & Hathaway, D. H. (2014a, August). Effects of meridional flow variations on solar cycles 23 and 24. *Astrophys. J.*, 792(2), 142. Retrieved from <https://doi.org/10.1088/0004-637X/792/2/142> doi: 10.1088/0004-637X/792/2/142

Upton, L., & Hathaway, D. H. (2014b, January). Predicting the Sun's Polar Magnetic Fields with a Surface Flux Transport Model. *Astrophys. J.*, 780, 5. doi: 10.1088/0004-637X/780/1/5

Wang, Y., & Sheeley, J. N. R. (1992, June). On Potential Field Models of the Solar Corona. *Astrophys. J.*, 392, 310–319. doi: 10.1086/171430

Welsch, B. T., Li, Y., Schuck, P. W., & Fisher, G. H. (2009, November). What is the Relationship Between Photospheric Flow Fields and Solar Flares? *Astrophys. J.*, *705*, 821-843. doi: 10.1088/0004-637X/705/1/821

Wheatland, M. S. (2005, July). A Statistical Solar Flare Forecast Method. *Space Weather*, *3*, 7003. doi: 10.1029/2004SW000131

Whitman, K., Egeland, R., Richardson, I. G., Allison, C., Quinn, P., Barzilla, J., ... Hosseinzadeh, P. (2023, December). Review of Solar Energetic Particle Prediction Models. *Advances in Space Research*, *72*(12), 5161-5242. doi: 10.1016/j.asr.2022.08.006

Woods, T. N., Kopp, G., & Chamberlin, P. C. (2006, October). Contributions of the solar ultraviolet irradiance to the total solar irradiance during large flares. *Journal of Geophysical Research (Space Physics)*, *111*(A10), A10S14. doi: 10.1029/2005JA011507

Xiao, H., Maloney, S., Krucker, S., Dickson, E., Massa, P., Lastufka, E., ... Piana, M. (2023, May). The data center for the Spectrometer and Telescope for Imaging X-rays (STIX) on board Solar Orbiter. *Astronomy and Astrophys.*, *673*, A142. doi: 10.1051/0004-6361/202346031

Zbinden, J., Kleint, L., & Panos, B. (2024, September). Investigating and comparing the IRIS spectral lines Mg II, Si IV, and C II for flare precursor diagnostics. *Astronomy and Astrophys.*, *689*, A72. doi: 10.1051/0004-6361/202347824